

Ultrahigh Extinction Ratio Long-Wave Infrared Polarization-Selective Broadband Metamaterial Absorber

Zheng Qin, Zhongzhu Liang,* Xiaoyan Shi, Dejia Meng, Rui Dai, Chunfang Sun, Wei Xin, Fuming Yang, Yingzheng Ren, and Jiajing Feng

Metamaterial absorbers (MAs) provide new miniaturization, integration, and high-performance solution for infrared polarization imaging systems. However, it is challenging for past MAs to obtain broadband absorption and a high extinction ratio simultaneously. Herein, a long-wave infrared broadband polarization-selective MA with an ultrahigh extinction ratio is proposed and numerically demonstrated. The MA is composed of a metal–dielectric–metal sandwich structure. The cut-wire resonator on the top layer and the wire pair on the bottom layer provide the MA with excellent polarization selectivity. In the wavelength range of 8.28–14.15 μm , the absorption of the Transverse Magnetic (TM) wave is greater than 90%, while the absorption of the Transverse Electric (TE) wave is less than 0.15%, and the average extinction ratio reaches 724. The high extinction ratio remains to reach 119 when the MA is integrated into a silicon substrate. This work promises to bring new solutions to infrared polarization imaging.


1. Introduction

Metamaterials are artificial structures with subwavelength-ordered arrangements. Their optical properties can be manipulated by changing the morphology and arrangement of their unit cells, thereby receiving extensive attention and research in

Z. Qin, Z. Liang, X. Shi, R. Dai, C. Sun
Center for Advanced Optoelectronic Functional Materials Research and Key Laboratory of UV Light-Emitting Materials and Technology of Ministry of Education, College of Physics
Northeast Normal University
Changchun 130024, China
E-mail: liangzz@nenu.edu.cn

Z. Qin
Interdisciplinary Center for Fundamental and Frontier Sciences
Nanjing University of Science and Technology
Jiangyin, Jiangsu 214443, China

Z. Qin, Z. Liang, X. Shi, D. Meng, W. Xin, F. Yang, Y. Ren, J. Feng
State Key Laboratory of Applied Optics
Changchun Institute of Optics, Fine Mechanics and Physics, Chinese Academy of Sciences
Changchun 130033, China

 The ORCID identification number(s) for the author(s) of this article can be found under <https://doi.org/10.1002/adpr.202200269>.

© 2022 The Authors. Advanced Photonics Research published by Wiley-VCH GmbH. This is an open access article under the terms of the Creative Commons Attribution License, which permits use, distribution and reproduction in any medium, provided the original work is properly cited.

DOI: 10.1002/adpr.202200269

recent years.^[1–4] Metamaterial absorbers (MAs) can concentrate and perfectly absorb incident light of target wavelength in a thickness much smaller than the wavelength,^[5] widely applied in solar energy-harvesting,^[6] thermal emitters,^[7] sensing,^[8,9] photoelectric detection,^[10] etc. Since the first MA working in the microwave band proposed in 2008,^[5] this subwavelength perfect absorption structure based on the patterned metal–dielectric–metal sandwich structure has been verified theoretically and experimentally in various wavelength bands from microwave to visible light.^[11–16]

Previous MA studying often focuses on only their spectral response range. These designs employ rotationally symmetric patterns to maximize the utilization of incident light energy to obtain polarization-

insensitive broadband or narrow-band absorption.^[15,17–20]

In recent years, polarization imaging and detection techniques have developed booming,^[21,22] and polarization-selective absorption has become increasingly important. Generally, the spontaneous emission and reflection of objects in the infrared band have polarization characteristics. Therefore, more abundant and multidimensional information can be obtained by detecting polarization state differences, thereby improving the detector's ability to identify targets in complex backgrounds. However, the traditional infrared focal plane cannot distinguish polarization information. To realize polarization detection, additional polarization optical components such as Woolaston prism, Glan-type polarizer, dichroic film polarizer, wire grid polarizer, etc. are required to modulate the incident light.^[23–26] These additional devices make the detection system bulky and complex.^[27] Integrated MAs enable infrared focal planes to obtain pixel-level spectral and polarization selectivity simultaneously, making it more compact and economical and avoiding the optical path alignment problem caused by the additional assembled device.^[28] The polarization-selective absorption of MAs is usually via the anisotropic resonator, such as asymmetric patterns or 1D grating patterns.^[10,28–33] For polarized elements, the extinction ratio, defined as the ratio of the intensity of two polarization parameters, is a critical performance parameter. In the infrared polarization imaging application of MAs, although the extinction ratio of a single wavelength can reach 136,^[34] the average extinction ratio of broadband is still less than 50,^[35] and the polarization selection ability is far inferior to existing polarimeters such as wire gratings.^[36]

Here, we propose a long-wave infrared polarization-selective metamaterial absorber (PSMA) configuration with wide operating bandwidth and ultrahigh extinction ratio. The three-layered PSMA consists of the top layer resonator array, the wire pair bottom, and a dielectric layer filled in the middle. The TM wave component of the incident light is coupled with the cut-wire resonator, excites the propagating and localized surface plasmon resonances (LSPRs), and induces high absorption to exceed 90% in the wavelength range of 8.28–14.15 μm . The absorption of the TE wave component is effectively suppressed below 0.15% owing to the polarization-selective response of the top resonator and bottom wire pair. Therefore, the PSMA has an excellent polarization-selective ability close to commercial metal gratings in the broad spectral range of long-wave infrared as its average extinction ratio reaches 724 (peak value 1700). The polarization-selective broadband absorption of our PSMA depends on the resonator and the underlying metal's topography. The broadband absorption and polarization selectivity are maintained when the PSMA is integrated into a transparent substrate. Our proposed PSMA may be a candidate for high-performance infrared polarization detection devices.

2. Modeling and Simulation

As shown in **Figure 1a**, our proposed PSMA consists of a three-layer structure of cut-wire resonator array–dielectric layer–metal wire pair. The geometric parameters of the PSMA are characterized by the unit period P , the resonator length L , the resonator width W_1 , the metal wire pair width W_2 , the intermediate gap g ,

the resonator thickness t , the dielectric layer thickness d , and the metal wire pair thickness t_b . Here, the material of the top resonator is titanium (Ti), the dielectric layer is silicon (Si), and the wire pair is aluminum (Al). These materials are commonly used in existing infrared devices and can be prepared by magnetron sputtering or electron beam evaporation. The top resonator array and underlying wire pair can be prepared by nanoprocessing methods such as electron beam lithography (EBL) and nanoimprinting. To characterize the performance of the metamaterial absorption, we performed a simulation using the finite-difference time-domain (FDTD) method. The material parameters of Al and Ti were obtained from Rakić,^[37] and the material parameters of Si were obtained from Palik,^[38] the optical parameters in the simulation band are shown in **Figure 1b**. In the simulation, the geometric parameters of the PSMA are set as: $P = 1.5 \mu\text{m}$, $L = 1.2 \mu\text{m}$, $W_1 = 200 \text{ nm}$, $g = 300 \text{ nm}$, $W_2 = 300 \text{ nm}$, $t = 50 \text{ nm}$, $d = 650 \text{ nm}$, and $t_b = 100 \text{ nm}$. The light is incident perpendicularly along the negative direction of the z -axis. Periodic boundary conditions are used in the x and y directions, and the perfectly matched layer (PML) boundary is used in the z -direction.

3. Optical Properties and Physical Mechanisms

When the incident light is a TM wave, which electric field vector is incident along the x -axis, parallel to the cut-wire resonator. As shown in **Figure 1c**, the absorption of PSMA is more than 80% in the wavelength range of 7.97–14.95 μm and exceeds 90% in the wavelength range of 8.28–14.15 μm . The absorption peaks are located at 8.95 and 13.1 μm , and the absorptivity reach

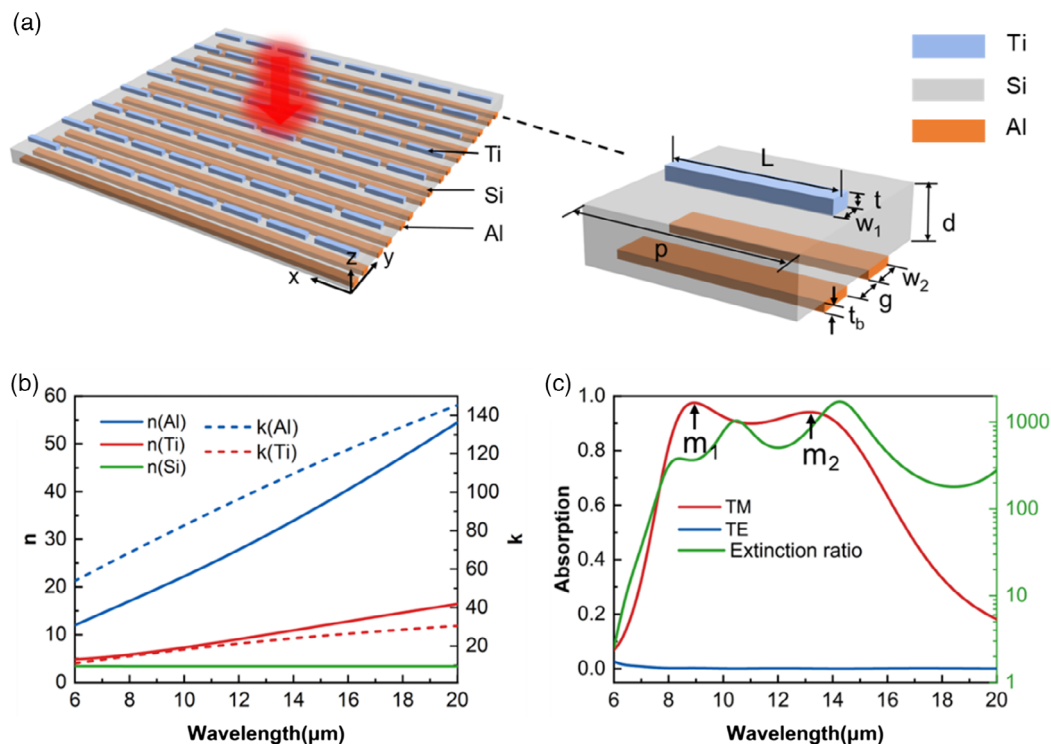


Figure 1. a) Schematic diagram of the configuration of PSMA. b) The optical parameters of Al, Ti, and Si (date from refs. [37,38]). c) The absorption spectrum and extinction ratio of PSMA.

97.5% and 94.1%, marked by m_1 and m_2 , respectively. When the TE wave is incident, the electric field vector along the y -axis is perpendicular to the cut-wire resonator. The absorption of the PSMA in the whole simulation band is less than 4%, and the absorptivity decreases with the wavelength increase. The absorptivity at the wavelength of $8\ \mu\text{m}$ is about 0.5%, and the average absorption in the wavelength range of $8.28\text{--}14.15\ \mu\text{m}$ is about 0.15%. The extinction ratio of a MA is defined as the ratio of the absorbed TM wave light intensity to the TE wave light intensity, which can be expressed as the ratio of the TM wave and TE wave absorptivity: $\eta(\lambda) = \frac{A(\lambda)_{\text{TM}}}{A(\lambda)_{\text{TE}}}$, and the average extinction ratio is expressed as: $\bar{\eta} = \frac{\int_{\lambda_1}^{\lambda_2} \eta(\lambda) d\lambda}{\int_{\lambda_1}^{\lambda_2} d\lambda}$. It can be seen from Figure 1c that the

maximum extinction ratio of the PSMA in the simulation band can reach 1700 (at $14.2\ \mu\text{m}$), and the average extinction ratio in the wavelength range of $8.28\text{--}14.15\ \mu\text{m}$ reaches 724. This value is much higher than previous reports,^[30,35] and our proposed PSMA polarization-selective ability is close to that of commercial polarization gratings.

To analyze the physical mechanism of broadband polarization-selective absorption, we plot the electric and magnetic field distributions at the two absorption peaks upon TM wave incidence in Figure 2. The electric and magnetic field distributions at corresponding wavelengths when TE waves are incident are also listed below. We marked the outline of the resonator in the figure with a white dashed line. Figure 2a shows the electric field distribution of the two absorption peaks of 8.95 and $13.1\ \mu\text{m}$ under TM wave incidence. It can be seen that the incident electric field is concentrated at the edges on both sides of the resonator, and its intensity at $13.1\ \mu\text{m}$ is about 3 times stronger than that at $8.95\ \mu\text{m}$. Figure 2b shows the cross section of the magnetic field distribution at the wavelengths of 8.95 and $13.1\ \mu\text{m}$ under TM wave incidence. The incident magnetic field is mainly concentrated near the upper and lower surfaces of the resonator. The difference between the two absorption peaks is that a part of the magnetic field at $8.95\ \mu\text{m}$ is concentrated near the upper surface of the wire pair below the two sides of the resonator, indicating that the propagating surface plasmon (PSP) is excited. At the wavelength of $13.1\ \mu\text{m}$, a part of the magnetic field is

concentrated in the dielectric layer just below the resonator, indicating that the localized surface plasmon (LSP) is excited. For PSP^[39]

$$\lambda_{\text{PSP}} = \frac{P}{\sqrt{\nu^2 + j^2}} \sqrt{\frac{\epsilon_m \epsilon_d}{\epsilon_m + \epsilon_d}} \quad (1)$$

Here, P is the period of the PSMA; ϵ_m and ϵ_d are the permittivity of metal and dielectric, respectively. The LSP can be explained by the equivalent circuit model^[40]

$$\lambda_{\text{LSP}} = 2\pi c \sqrt{LC/2} \quad (2)$$

Here, L and C are the equivalent inductance and equivalent capacitance. The equivalent inductance depends on the dielectric constant of the material and the distance between the two layers of metal and has $L \propto d$. For equivalent capacitance, $C \propto \frac{1}{d}$ and $C \propto \frac{1}{P}$.

When the TE wave is incident, the cut-wire resonator does not generate surface plasmon resonance in the simulated wavelength range. As shown in Figure 2c,d, neither the incident electric field nor the magnetic field has a noticeable concentration effect. On the other hand, as the duty cycle of the underlying wire pair is small and the size in the y -direction is much smaller than the wavelength ($< 1/20\ \lambda$), it cannot support efficient reflection, and cavity modes cannot be excited here. In addition, silicon is a lossless dielectric in long-wave infrared, so there is no appreciable absorption of TE wave in the whole simulated wave band.

Next, we analyze the effect of the geometric parameters of the resonator on the performance of PSMA. Figure 3a shows that as the length of the resonator increases, m_2 produces a noticeable redshift while the position of m_1 maintains. As predicted by Equation (2), the MA's equivalent capacitance increases with the resonator's length, resulting in a redshift of the LSPR. Figure 3b shows that the change in the resonator length little affects the absorption of the TE wave and the absorption spectrum of the three cases with different values of the resonator length overlap entirely. As shown in Figure 3c, as the period increases, m_1 has a redshift, which is in line with the prediction

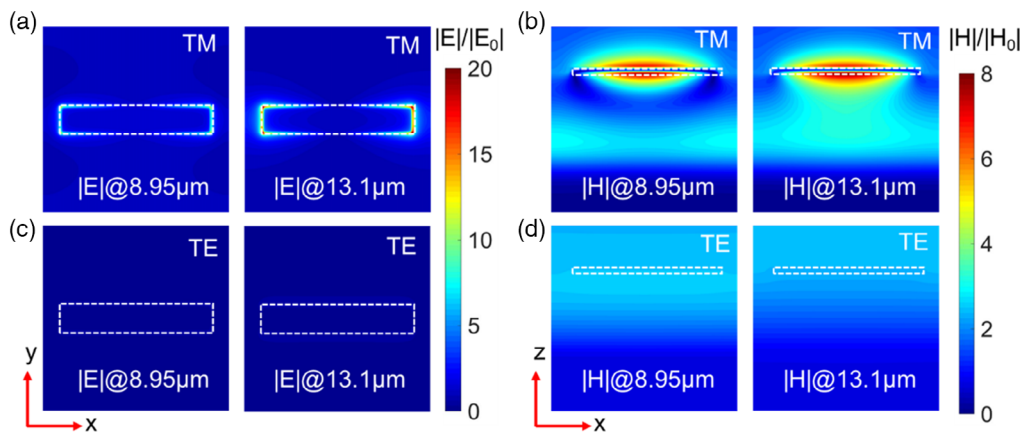


Figure 2. a) The electric field distribution at the two absorption peaks of the TM wave incident, b) the magnetic field distribution at the two absorption peaks of the TM wave incident, and c) the electric field distribution at the corresponding wavelength of the TE wave incident, d) the magnetic field distribution at the corresponding wavelength of the TE wave incident.

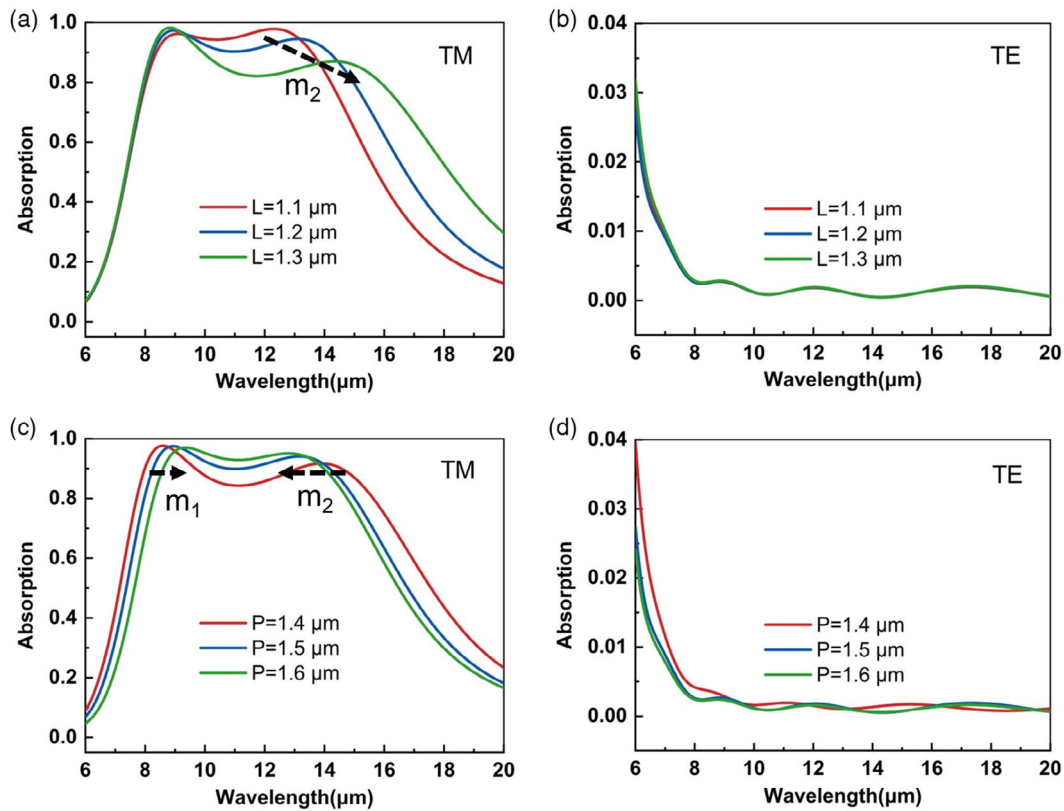


Figure 3. a) The dependence of the TM wave absorption spectrum on resonator length, b) the dependence of the TE wave absorption spectrum on resonator length, c) the dependence of the TM wave absorption spectrum on resonator width, and d) the dependence of the TE wave absorption spectrum on resonator width.

of Equation (1). And m_2 produces a blueshift owing to PSMA's equivalent capacitance decreasing with the period's increase (according to Equation (2)). Due to the opposite movement of m_1 and m_2 , the absorption bandwidth of PSMA also decreases with the period increasing. Figure 3d shows that the absorption of the TE wave slightly decreases as the period increases, which is due to the decrease in the duty cycle of the underlying wire pair as the period increases.

4. Influence of Top and Underlying Metal Patterns on the Performance of PSMA

As mentioned above, the size change of the resonator has little effect on the polarization-selective ability of PSMA. Next, we will analyze the effect of the resonator and underlying metal topography.

Figure 4 shows the dependence of PSMA performance on the top resonator pattern. Figure 4a shows that we consider three resonator patterns: cross-shaped, I-shaped, and T-shaped. The length of the three patterns is equal to the length of the cut-wire resonator, $L_1 = L = 1.2 \mu\text{m}$, the width is the same as that of the resonator, and the short axis length of the I-shaped resonator is $L_2 = 0.6 \mu\text{m}$. The absorption spectrum of the incident TM wave is shown in Figure 4b. It can be seen that the absorption of the cross-shaped resonator almost coincides with the cut-wire

resonator, indicating that the existence of the longitudinal axis of the cross-shaped resonator hardly affects the absorption of the TM wave. Compared with the cut-wire resonator, the m_1 of the I-shaped resonator and the T-shaped resonator has almost no change, while the m_2 has a significant redshift, and the absorptivity decreases. The electric dipole resonance generated by the coupling of the incident TM wave and the resonator makes the incident electric field concentrated at both ends of the resonator, so the topography changes at both ends of the resonator can significantly affect its LSPR. Although the I- and T-shaped resonators are only elongated in the y -direction relative to the cut-wire resonators, the effective length of the resonators increases significantly, so the LSPR peaks (m_2) are redshifted. The absorption spectrum of the incident TE wave is shown in Figure 4c. It can be seen that the absorption of the TE wave of the three pattern resonators is significantly increased compared with the cut-wire resonator. The absorption of the cross- and T-shaped resonator structures is more than 4% in the whole simulation band and close to 20% at the wavelength of $6 \mu\text{m}$. The absorption of the I-shaped resonator structure is slightly higher than that of the cut-wire resonator in the wavelength longer than $10 \mu\text{m}$, while it is significantly elevated in the wavelength band less than $10 \mu\text{m}$ and reaching 34% at the wavelength of $6 \mu\text{m}$. Therefore, only cut-wire resonators can achieve broadband polarization-selective absorption with high extinction ratios.

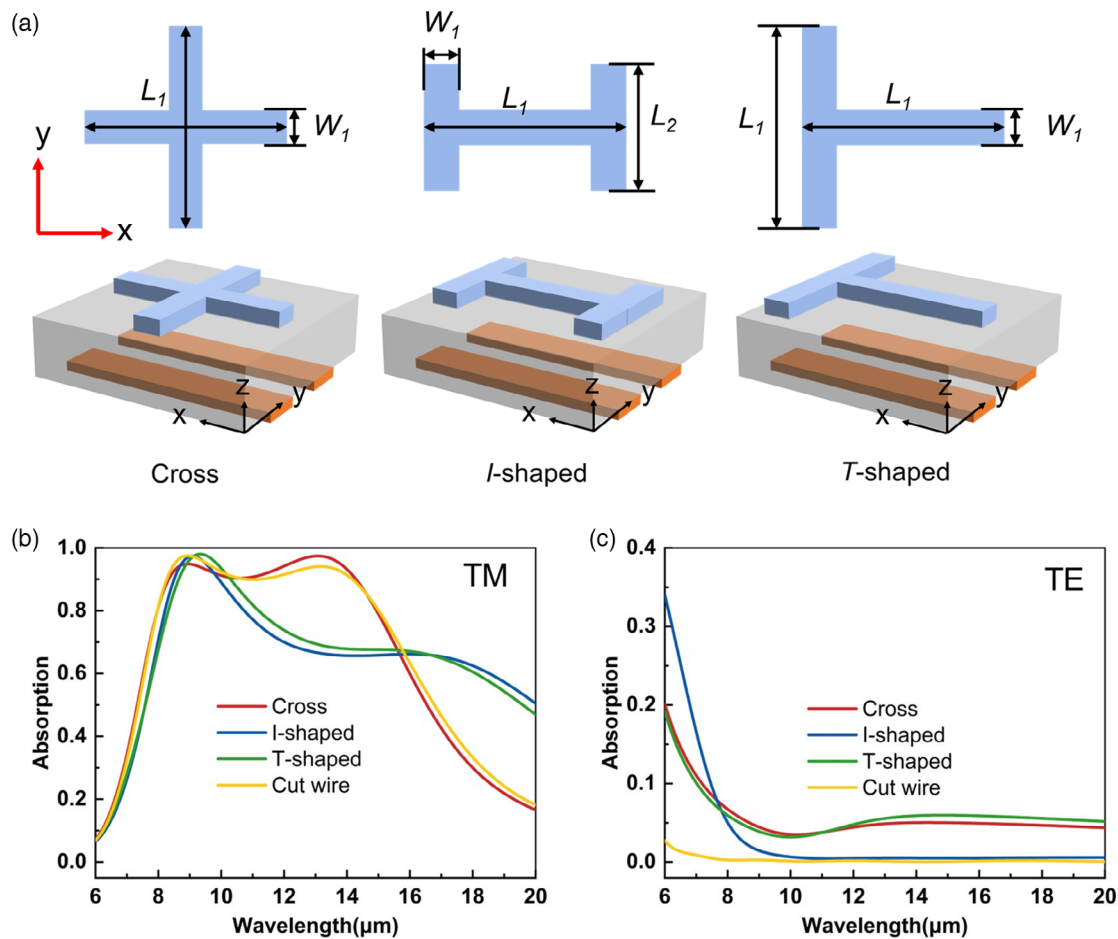


Figure 4. Optical properties of MAs with different resonator patterns. a) Schematic diagram of three resonator patterns, b) absorption spectrum of TM wave, and c) absorption spectrum of TE wave.

Figure 5 shows the dependence of PSMA performance on the underlying metal pattern. Figure 5a shows that we consider three cases of underlying layer: a rectangular hole at the corresponding position of the resonator, a strip grating directly below the cut-wire resonator, and a continuous layer (plane). Here, the width of the rectangular hole and the stripe grating equals the gap of the wire pair (Figure 1a), $g = 300$ nm. The length of the rectangular hole is equal to the cut-wire resonator, $L_3 = L = 1.2$ μm . It can be seen in Figure 5b that the rectangular hole configuration and the continuous layer configuration exhibit broadband absorption, and the positions of the two absorption peaks are slightly blueshifted relative to the wire pair configuration. Meanwhile, the two absorption peaks of the stripe grating configuration have noticeable redshifts relative to the metal wire pair configuration, and the absorptivity of the m_1 has dropped significantly. The absorption spectrum of the incident TE wave is shown in Figure 5c, and the absorption spectrum of the stripe grating configuration almost coincides with the wire pair configuration. The continuous layer configuration excites an F–P cavity mode at the wavelength of 9.1 μm with an absorptivity of 16%. The rectangular hole configuration excites a new resonance mode and couples with the F–P cavity mode, resulting in the absorptivity

at the wavelength of 10.5 μm (absorption peak) reaching 30%, and the absorptivity at 6 μm is close to 50%. The continuous layer and the rectangular hole configuration noticeably lack polarization selectivity due to the noticeable absorption of TE waves. The duty cycle of the underlying metal pattern indeed determines the polarization selectivity of PSMA. Despite the stripe grating configuration having low TE wave absorption, its TM wave absorption is lower than that of the wire pair configuration.

For more, we calculate the performance of PSMA when the lower metal wire pairs take different values. Figure 6a shows the absorption spectrum of the TM wave. When $W_2 = 200$ nm, the working wave band of PSMA redshift (relative to $W_2 = 300$ nm) and the $A > 90\%$ wavelength range is 9–14.75 μm . When $W_2 = 400$ nm, the working wave band of PSMA blueshift (relative to $W_2 = 300$ nm) and the $A > 90\%$ wavelength range is 7.92–113.6 μm . Figure 6b shows the absorption spectrum of the TE wave. The PSMA's absorption to the TE wave decreases with the decrease of the wire pair's width (duty cycle). Accordingly, as shown in Figure 6c, PSMA's extinction ratio increases with the wire pair's width (duty cycle) decrease to a certain extent. When $W_2 = 200$ nm, PSMA's average extinction ratio in the wavelength range at 9–114.75 μm reaches more than 1300.

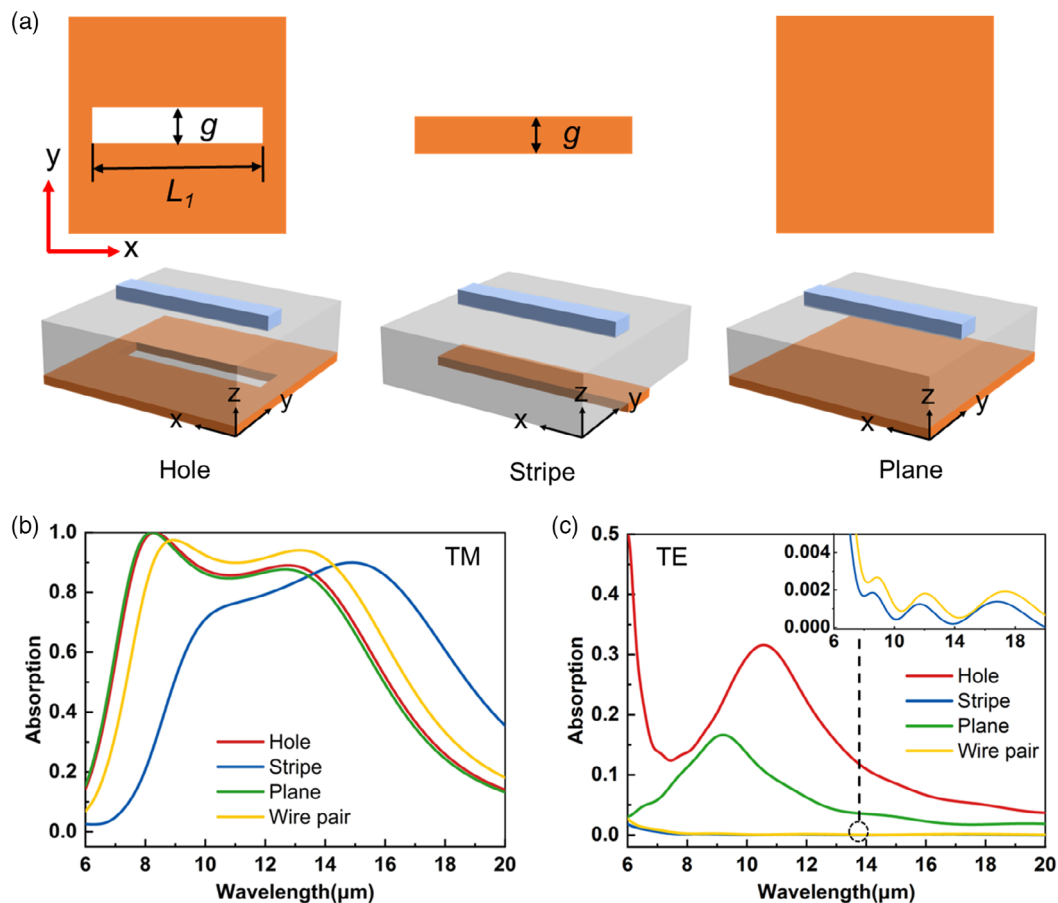


Figure 5. Optical properties of MAs with different underlying metal patterns. a) Schematic diagram of three underlying metal patterns, b) TM wave absorption spectrum, and c) TE wave absorption spectrum.

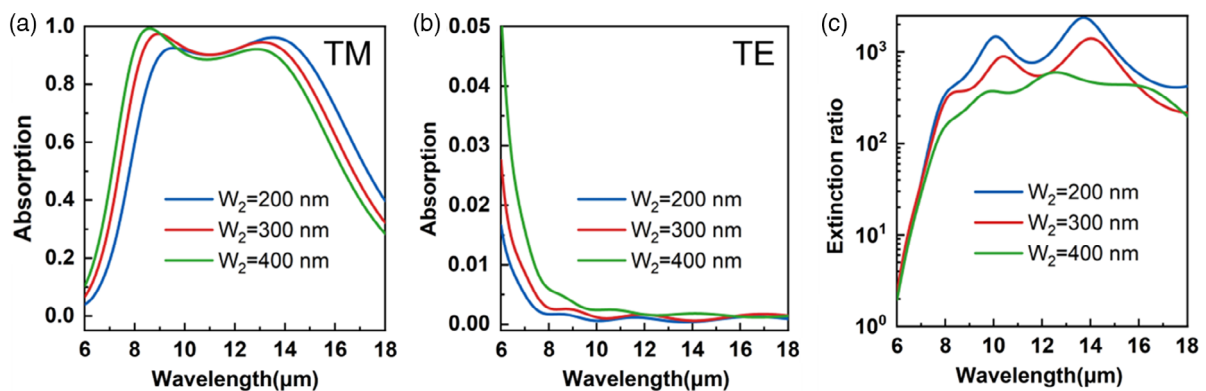


Figure 6. Optical properties of PSMA with different values of W_2 . a) TM wave absorption spectrum, b) TE wave absorption spectrum, and c) the extinction ratio of the MA.

When $W_2 = 400$ nm, the average extinction ratio of PSMA in the wavelength range at 7.92–113.6 μm decreases to 398. Although PSMA obtained a higher extinction ratio when $W_2 = 200$ nm, its TM wave absorption bandwidth and average absorptivity slightly decreased.

5. With a Substrate

In the previous simulations and calculations, we only considered the metal–dielectric–metal three-layer structure, that is, the case where there is no substrate under PSMA. For general MAs, the

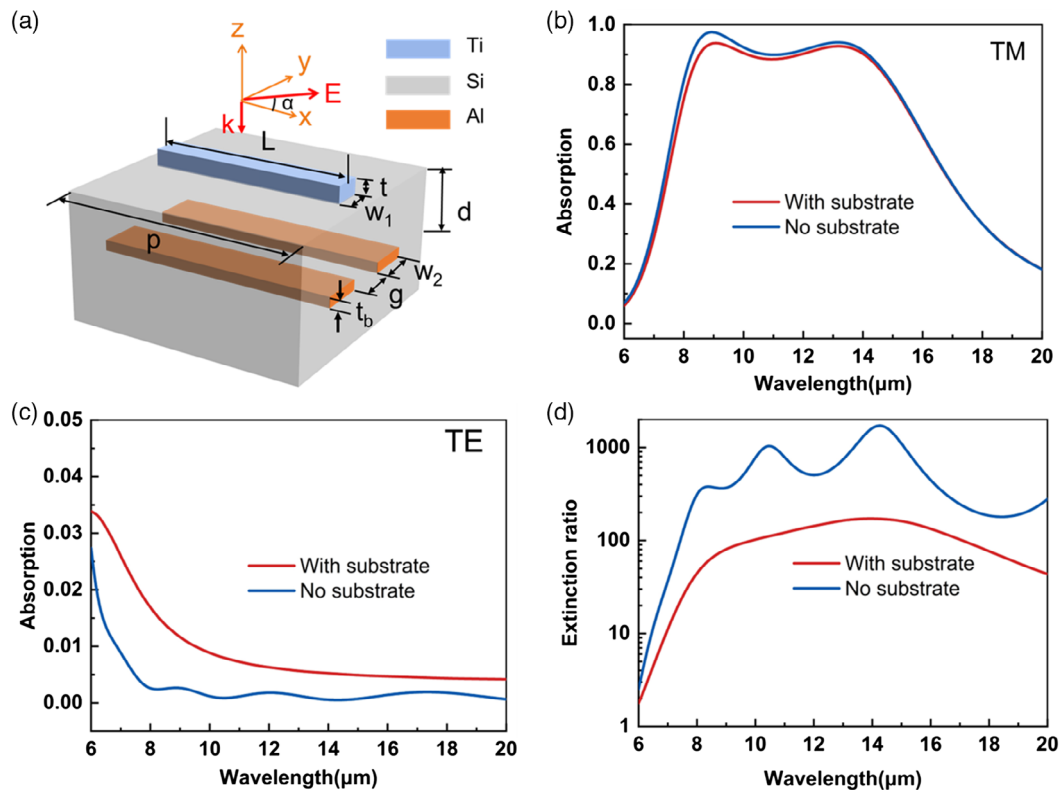


Figure 7. a) Schematic diagram of the configuration of PSMA with silicon substrate, b) the TM wave absorption spectrum of PSMA, c) the TE wave absorption spectrum of PSMA, d) the extinction ratio spectrum of PSMA.

underlying metal is a continuous layer thick enough to block any incident light's penetration, so the underlying substrate's influence is not considered in calculations and analyses. When the underlying metal is no longer a continuous plate, it cannot wholly block the penetration of incident light, whether for TM or TE waves. In this condition, we need to consider the interaction of the incident light with the medium (substrate) below the underlying metal.

As shown in **Figure 7a**, we added a silicon substrate (300 μm) much thicker than the wavelength below the structure of **Figure 1a**, and considering the practical fabrication, the wire pairs are wrapped in the silicon substrate. **Figure 7b** shows the absorption spectrum of the incident TM wave. It can be seen that the existence of the substrate has almost no effect on the absorption of the TM wave, and the absorptivity of the with-substrate configuration in the wavelength range of 8.17–14.67 μm is greater than 85%. **Figure 7c** shows the absorption spectrum of the incident TE wave. It can be seen that the absorption of the TE wave with the with-substrate configuration is improved compared with the without-substrate configuration. The absorptivity of the PSMA reaches 3.3% at the wavelength of 6 μm , 1.7% at 8 μm , and 0.4% at the longer wavelength. Due to the increased absorption of the TE wave, the extinction ratio of the with-substrate configuration is less than that of the without-substrate structure. As shown in **Figure 7d**, the average extinction ratio of the with-substrate configuration in the wavelength range of 8.17–14.67 μm drops to 119.

6. Conclusion

We propose a broadband PSMA design with an ultrahigh extinction ratio. The cut-wire resonator–dielectric layer–wire pair sandwich structure exhibit high absorption exceeding 90% of TM wave in the wide wavelength range of 8.28–14.15 μm and significantly low absorption of TE wave, and then ultrahigh extinction ratio with an average value of 724 is obtained. The broadband absorption of TM waves is owing to the simultaneous excitation of PSPR and LSPR. In contrast, the low absorption of TE waves benefits from the polarization-selective properties of cut-wire resonators and the underlying wire pair. The resonator pattern and the underlying metal pattern determine the broadband polarization-selective capability of PSMA. When PSMA is integrated into a silicon substrate, the broadband absorption and high extinction ratio can still be maintained. Our proposed PSMA is expected to be applied in infrared polarization detection and thermal polarization emitters.

Acknowledgements

This work was funded by the National Natural Science Foundation of China (grant nos. 61735018 and 61805242); Scientific and Technological Development Project of Jilin Province (grant no. 20220201080GX); Excellent Member of Youth Innovation Promotion Association of the Chinese Academy of Sciences (grant nos. 2014193 and Y201836); and Leading Talents and Team Project of Scientific and

Technological Innovation for Young and Middle-aged Groups in Jilin Province (grant no. 20190101012JH).

Conflict of Interest

The authors declare no conflict of interest.

Data Availability Statement

The data that support the findings of this study are available from the corresponding author upon reasonable request.

Keywords

infrared polarization imaging, long-wave infrared, metamaterial absorbers, polarization-selective absorber

Received: September 24, 2022

Revised: October 21, 2022

Published online: January 8, 2023

- [1] T. J. Cui, M. Q. Qi, X. Wan, J. Zhao, Q. Cheng, *Light Sci. Appl.* **2014**, *3*, e218.
- [2] W. J. Padilla, R. D. Averitt, *Nat. Rev. Phys.* **2022**, *4*, 85.
- [3] Z. Xuan, J. Li, Q. Liu, F. Yi, S. Wang, W. Lu, *Innovation* **2021**, *2*, 100081.
- [4] S. A. Khan, N. Z. Khan, Y. Xie, M. T. Abbas, M. Rauf, I. Mehmood, M. Runowski, S. Agathopoulos, J. Zhu, *Adv. Opt. Mater.* **2022**, *10*, 2200500.
- [5] N. I. Landy, S. Sajuyigbe, J. J. Mock, D. R. Smith, W. J. Padilla, *Phys. Rev. Lett.* **2008**, *100*, 207402.
- [6] C. Fei Guo, T. Sun, F. Cao, Q. Liu, Z. Ren, *Light Sci. Appl.* **2014**, *3*, e161.
- [7] P. Torma, W. L. Barnes, *Rep. Prog. Phys.* **2015**, *78*, 013901.
- [8] C. Chen, G. Wang, Z. Zhang, K. Zhang, *Opt. Lett.* **2018**, *43*, 3630.
- [9] X. Tan, H. Zhang, J. Li, H. Wan, Q. Guo, H. Zhu, H. Liu, F. Yi, *Nat. Commun.* **2020**, *11*, 5245.
- [10] W. Li, Z. J. Coppens, L. V. Besteiro, W. Wang, A. O. Govorov, J. Valentine, *Nat. Commun.* **2015**, *6*, 8379.
- [11] C. Hu, Z. Zhao, X. Chen, X. Luo, *Opt. Express* **2009**, *17*, 11039.
- [12] H. Tao, N. I. Landy, C. M. Bingham, X. Zhang, R. D. Averitt, W. J. Padilla, *Opt. Express* **2008**, *16*, 7181.
- [13] J. Hao, J. Wang, X. Liu, W. J. Padilla, L. Zhou, M. Qiu, *Appl. Phys. Lett.* **2010**, *96*, 251104.
- [14] X. Liu, T. Starr, A. F. Starr, W. J. Padilla, *Phys. Rev. Lett.* **2010**, *104*, 207403.
- [15] N. Liu, M. Mesch, T. Weiss, M. Hentschel, H. Giessen, *Nano Lett.* **2010**, *10*, 2342.
- [16] L. Ye, Y. Chen, G. Cai, N. Liu, J. Zhu, Z. Song, Q. H. Liu, *Opt. Express* **2017**, *25*, 11223.
- [17] Y. Zhou, Z. Qin, Z. Liang, D. Meng, H. Xu, D. R. Smith, Y. Liu, *Light Sci. Appl.* **2021**, *10*, 138.
- [18] Z. Qin, C. Zhang, Z. Liang, D. Meng, X. Shi, F. Yang, *Adv. Photonics Res.* **2022**, *3*, 2100215.
- [19] Y. Wang, H.-X. Xu, C. Wang, H. Luo, S. Wang, M. Wang, *Adv. Photonics Res.* **2022**, 2200063.
- [20] B. Zhang, K.-D. Xu, *J. Opt. Soc. Am. B* **2022**, *39*, A52.
- [21] N. A. Rubin, G. D'Aversa, P. Chevalier, Z. Shi, W. T. Chen, F. Capasso, *Science* **2019**, *365*, eaax1839.
- [22] A. Basiri, X. Chen, J. Bai, P. Amrollahi, J. Carpenter, Z. Holman, C. Wang, Y. Yao, *Light Sci. Appl.* **2019**, *8*, 78.
- [23] G. Kristan, F. Melvin, M. Robert, L. Daniel, F. Craig, K. Michael, P. Larry, presented at *Proc. SPIE*, **2010**.
- [24] K. J. Voss, Y. Liu, *Appl. Opt.* **1997**, *36*, 6083.
- [25] K. J. Voss, N. Souaidia, *Opt. Express* **2010**, *18*, 19672.
- [26] W. K. Michael, J. L. Pezzaniti, L. D. Eustace, R. G. Grant, "Infrared Stokes imaging polarimeter using microbolometers", presented at *Proc. SPIE*, **2009**.
- [27] M. Dai, C. Wang, B. Qiang, F. Wang, M. Ye, S. Han, Y. Luo, Q. J. Wang, *Nat. Commun.* **2022**, *13*, 4560.
- [28] J. Li, L. Bao, S. Jiang, Q. Guo, D. Xu, B. Xiong, G. Zhang, F. Yi, *Opt. Express* **2019**, *27*, 8375.
- [29] L. Zhang, Y. Zheng, J. Zhang, Y. Yin, Q. Li, J. Lei, Y. Zhu, *Opt. Express* **2021**, *29*, 21473.
- [30] Y. K. Zhong, S. M. Fu, W. Huang, D. Rung, J. Y. Huang, P. Parashar, A. Lin, *Opt. Express* **2017**, *25*, A124.
- [31] a) Z. Lin, Z. Xu, P. Liu, Z. Liang, Y.-S. Lin, *Opt. Laser Technol.* **2020**, *121*, b) Z. Lin, Z. Xu, P. Liu, Z. Liang, Y.-S. Lin, *Opt. Laser Technol.* **2020**, *121*, 105826.
- [32] Z. Cui, D. Zhu, L. Yue, H. Hu, S. Chen, X. Wang, Y. Wang, *Opt. Express* **2019**, *27*, 22190.
- [33] P. K. Venuthurumilli, P. D. Ye, X. Xu, *ACS Nano* **2018**, *12*, 4861.
- [34] Y. W. Zhou, Z. F. Li, J. Zhou, N. Li, X. H. Zhou, P. P. Chen, Y. L. Zheng, X. S. Chen, W. Lu, *Sci. Rep.* **2018**, *8*, 15070.
- [35] S. Jiang, J. Li, J. Li, J. Lai, F. Yi, *Opt. Express* **2022**, *30*, 9065.
- [36] <https://www.thorlabschina.cn/thorproduct.cfm?partnumber=WP25M-IRC>
- [37] A. D. Rakić, A. B. Djurišić, J. M. Elazar, M. L. Majewski, *Appl. Opt.* **1998**, *37*, 5271.
- [38] E. D. Palik, *Handbook of Optical Constants of Solids*, Vol. 3, Academic Press **1998**.
- [39] C. Genet, T. W. Ebbesen, *Nature* **2007**, *445*, 39.
- [40] Y. Q. Ye, Y. Jin, S. He, *J. Opt. Soc. Am. B* **2010**, *27*, 498.